When JV Curves Conceal Material Improvements: The Relevance of Photoluminescence Measurements in the Optimization of Perovskite Solar Cells

Chris Dreessen, Kassio P. S. Zanoni, Lidón Gil-Escrig, Nathan Rodkey, Jafar I. Khan, Frédéric Laquai, Michele Sessolo, Cristina Roldán-Carmona,* and Henk J. Bolink*

Lead halide perovskites have prompted great interest, offering impressive photovoltaic performances. Most fundamental investigations and cell optimizations focus on solution-based solar cells, which are not easily extended to larger scales. Commonly in these cells, losses in the open-circuit voltage are attributed to arise primarily from interface recombination, and therefore the most studies have focused on optimization of the surface to eliminate defects states. In contrast, thermal evaporation is an alternative, solvent-free, and scalable method to deposit lead halide perovskites that is gaining attention. However, the number of reports showing high-efficiency solar cells (> 20%) prepared using thermal evaporation is still small. Here, the origins of non-radiative charge carrier recombination are investigated in perovskite cells that are deposited via thermal co-evaporation. This is done through a combination of photoluminescence spectroscopy, current-voltage characterization, and simulations. It is found that the non-radiative recombination in these cells is caused equally by bulk and interface defects. In general, it is advocated to perform a dual analysis of the photoluminescence spectroscopy of both the film and the photovoltaic device, in conjunction with current-voltage measurements. It is emphasized that such a dual analysis is needed to enable the identification of improvements and to unlock further advancements in this technology.

1. Introduction

Metal-halide perovskites have become one of the most promising emerging semiconductor materials for photovoltaics and other optoelectronic technologies. In the span of a decade, they have demonstrated significant breakthroughs in power conversion efficiency (PCE) and operational stability, recently reaching a certified record PCE of 26.1%.[1] These advancements are caused by a high absorption coefficient, long carrier diffusion lengths, and high tolerance to chemical defects. Additionally, features such as a facile bandgap tunability and versatility in crystalizing as high-quality materials from a variety of film deposition techniques have prompted further interest in the community.[2–5]

To reach very high efficiency, perovskite solar cells (PSCs) should have minimum open-circuit voltage (V_{oc}) losses, which implies reducing the non-radiative recombination of the photogenerated charges. Non-radiative recombination can happen either inside the perovskite bulk material or at the interface with the charge transport layers (CTLs), and is generally quantified by the photoluminescence quantum yield (PLQY). The latter is directly related to the quasi-Fermi level splitting (QFLS) or V_{oc}, so that a reduction in radiative recombination implies a loss in QFLS or V_{oc}. To date, perovskite films with outstanding external PLQYs up to 66%, indicating internal PLQYs close to 100%, have been reported.[6–12] Such high PLQY values

C. Dreessen, K. P. S. Zanoni, L. Gil-Escrig, N. Rodkey, M. Sessolo, C. Roldán-Carmona, H. J. Bolink
Instituto de Ciencia Molecular
ICMol
Universidad de Valencia
C/Catedrático J. Beltrán 2, Paterna 46980, Spain
E-mail: cristina.roldan@uv.es; henk.bolink@uv.es

J. I. Khan, F. Laquai
KAUST Solar Center (KSC)
Physical Sciences and Engineering Division (PSE)
Material Science and Engineering Program (MSE) and Applied Physics (AP) Program
King Abdullah University of Science and Technology (KAUST)
Thuwal 23955-6900, Kingdom of Saudi Arabia

**ADVANCED
SCIENCE NEWS**

www.advancedsciencenews.com

**ADVANCED
OPTICAL
MATERIALS**

www.advopticalmat.de

are obtained mostly for solution processed films, the most widely-adopted perovskite absorbers, and demonstrate their potential to reach a PCE above 28%.[13] This is not completely surprising given that most defects in the bulk of perovskites lead to shallow trap states,[14,15] that induce minimal non-radiative charge carrier recombination. In addition, solution-processed perovskites often exhibit large micrometer-sized grains, hence they are less affected by recombination centers at the grain boundaries.[7,16–18] In view of the high PLQY values obtained for thin perovskite films, and the strong reduction observed after contacting to the CTLs, the consensus is that non-radiative recombination at the perovskite interfaces is the major loss factor. As a result, there has been a strong focus on understanding and suppressing interface recombination at the CTLs. Indeed, a prevailing strategy to improve device efficiency involves the screening of alternative CTLs and/or the introduction of passivating interlayers at the absorber surface.[13,19–30]

In spite of the predominance of solution-processed perovskites, alternative solvent-free coating technologies are emerging as promising routes given their potential for scalability and reproducibility.[31,32] One of the solvent-free methods for perovskite deposition is thermal evaporation of the perovskite precursors. It offers accurate control of the film thickness and composition and it enables the formation of multilayer stacks on a variety of substrates.[33–36] Using thermal evaporation, PCSs with PCEs up to 21.3% have been reported employing different perovskite compositions in both p-i-n and n-i-p configurations, on flexible substrates and also semitransparent devices.[37–41] Very recently, a record PCE of 24.4% (certified 22.6%) based on sequentially evaporated, $PbCl_2$-alloyed $Cs_{0.05}FA_{0.95}PbI_3$ was reported.[42] Yet, in general, thermally evaporated perovskites are still poorly understood. As a result, only a few reports of PSCs using co-evaporated precursors show PCEs above 20%.[43,44] This opens the debate on the dominating recombination centers in evaporated PSCs. Indeed, thermally evaporated perovskites typically consist of small crystal grains, which leads to more grain boundaries and structural defects than their solution-processed analogs.[32] It is therefore expected that they suffer from higher recombination losses, which would explain the short charge-carrier lifetimes that are reported for these films.[45]

Here, we study the origin of trap-assisted recombination in thermally co-evaporated solar cells based on the archetypal methylammonium lead iodide ($MAPbI_3$) perovskite. We obtain the PLQY and study the excited state decay time of the perovskite film on glass and solar cells with a variety of interface layers. Additionally, we compare the measured current density versus voltage curves under 1 sun illumination (JV_{sun}) with pseudo-JV curves constructed from light-intensity dependent data. Through these experimental results and device simulations, we describe the interplay between bulk and interface recombination, and provide a comprehensive picture of the performance limitations in co-evaporated cells. Contrary to what is generally observed in solution-based perovskites, here we find that trap-assisted recombination in thermally co-evaporated cells does not occur predominantly at the interfaces with the CTLs, instead the bulk quality of co-evaporated perovskites is equally limiting the V_{oc}. Such a dual contribution, unusual in state-of-the-art solution-processed PSCs, must be carefully considered before any device optimization, as it leads to a minimal response of the JV curve

once isolated improvements in non-radiative recombination are achieved. As an example, enhancements due to interface passivation when screening different materials will likely be insignificant regarding V_{oc} changes if the bulk limitation is not considered. As a consequence, the analysis of JV_{sun} curves alone performed in many optimization processes is insufficient, and may be hindering important advancements in vacuum-processed PSCs. As a solution, we recommend adopting a combined approach which compares the photoluminescence (PL) of the perovskite film and that of the full device, in addition to the JV_{sun} curve. Such a dual characterization protocol provides an easy and accessible way for many laboratories to disentangle the relative contribution of bulk and interface recombination, and thus detect any material improvements during device optimization. Importantly, this strategy is not only recommended for co-evaporated perovskites with moderate PCE, but for all types of solar cells once the interfaces are optimized to the perovskite-bulk limit.

2. Results and Discussion

2.1. Status-Quo of Co-Evaporated PSCs

PSCs were prepared by thermal evaporation using a planar n-i-p configuration, consisting of $ITO/SnO_2/C_{60}$ and $TaTm/TPBi/MoO_3/Ag$ as electron and hole extraction contacts, as previously reported by our group,[46] respectively, with C_{60} being the buckminsterfullerene, TaTm being N,N,N′,N′-Tetra([1,1′-biphenyl]—4-yl)[1,1′:4′,1″-terphenyl]—4,4″-diamine, and TPBi being 2,2′,2″-(1,3,5-benzinetriyl)-tris(1-phenyl-1-H-benzimidazole) (see methodology for further details). The perovskite films were prepared by co-sublimation of the MAI and PbI_2 precursors and summarized in the methodology section. **Figure 1**a provides the cross sectional scanning electron microscopy (SEM) image of a typical device. The $MAPbI_3$ film exhibits a heterogeneous morphology containing multiple crystal grain sizes, some column-like with a length of $\approx 300 - 400$ nm, others smaller than 100 nm. This implies that during extraction, charge carriers need to pass several grain boundaries in the vertical direction, increasing the probability of recombining at trap centers. Charge carrier recombination leads to losses in the V_{oc}. An example of a typical JV_{sun} curve of a co-evaporated $MAPbI_3$ solar cell is shown in Figure 1b (see the statistics of the parameters in Figure S9, Supporting Information). The V_{oc} is close to 1.13 V which is higher than the average reported value for solution-processed $MAPbI_3$ solar cells 1.09 V, (extracted from the Perovskite Database, data from 1/14 until 1/21, PCE > 18%),[43] where larger crystal grains are usually reported.[17,18] A V_{oc} of 1.13 V is, however, significantly below than what is theoretically expected for a solar cell based on $MAPbI_3$. It is therefore important to understand the origin of the V_{oc} losses in co-evaporated perovskite cells and identify means to reduce them.

To investigate the sources of the V_{oc} losses we performed PLQY measurements. This technique allows the photoexcitation of a sample with just one layer or a combination of layers, and therefore it enables the selective probing of possible recombination centers in a full device. We performed a comparative analysis of the PLQY for the perovskite film deposited on glass and for the entire device. The prior represents the limiting case
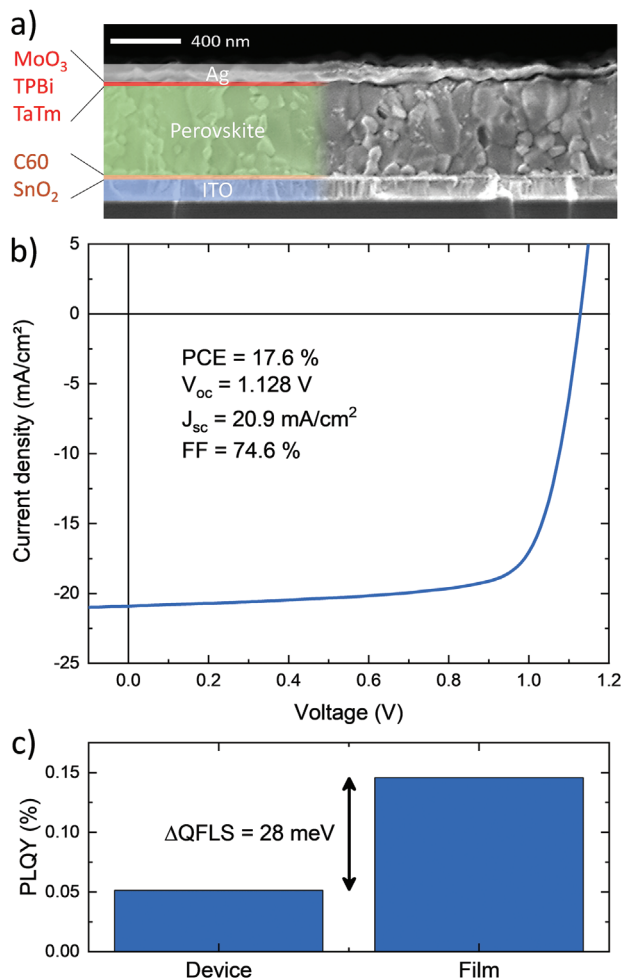
**ADVANCED
SCIENCE NEWS**

www.advancedsciencenews.com

**ADVANCED
OPTICAL
MATERIALS**

www.advopticalmat.de

Figure 1. a) Cross sectional SEM image of a typical co-evaporated *n-i-p* MAPbI$_3$ solar cell. b) JV_{sun} curve of a typical co-evaporated PSC, shown in *a*. c) PLQY comparison under 1-sun equivalent illumination between a full device and glass/perovskite film and the corresponding difference in QFLS.

in which recombination is only happening in the perovskite bulk, considering that recombination at the interfaces with glass and N$_2$ can be neglected (later verified in Section 2.2). To enhance readability, we will refer to the parameters measured on the film on glass with the subscript "film" and to the parameters measured on the full device with the subscript "device". We note that the V_{oc} is always measured on the full device. Assuming that the reciprocity relation is fulfilled,[47] the PLQY directly relates to the quasi-Fermi level splitting via

$$QFLS = qV_{oc,rad}\left(E_g\right) + kT \ln\left(PLQY\right) \qquad (1)$$

where $V_{oc,rad}$ is the radiative limit of the V_{oc} given by the Shockley-Queisser limit (SQ), which is most accurately determined via the external quantum efficiency of the solar cell.[48] E_g is the bandgap of the perovskite and k, T and q are the Boltzmann constant, the temperature of the charge carriers, and the elementary charge, respectively. The QFLS refers to the splitting of the quasi-Fermi levels of the electrons and holes in the perovskite bulk, and cor-

responds to qV_{oc} when measured on the full device with aligned band energies.[20] We first consider a MAPbI$_3$ film fabricated by thermal co-evaporation on top of a glass substrate, and compare it to the film embedded in a full device architecture. Following Figure 1c and Equation 1, a value of PLQY$_{film}$ = 0.146% corresponds to QFLS$_{film}$ = 1.157 eV, and PLQY$_{device}$ = 0.051% corresponds to QFLS$_{device}$ = 1.130 eV, with a reasonable agreement to the V_{oc} = 1.128 V. According to the literature, the passivated free standing perovskite films (that is glass/perovskite film exposed to N$_2$) are generally more luminescent than the full devices.[13,19–30] This indicates that the V_{oc} losses are indeed dominated by recombination at the CTLs interfaces. However, this is mostly reported for solution-processed perovskites. In our co-evaporated MAPbI$_3$ films we only observe a slight difference in PLQY (factor of 3) between free-standing MAPbI$_3$ films and the completed solar cells. The observed difference would correspond to a small voltage reduction of $\approx$0.028 V (see Figure 1c; Figure S1a, Supporting Information). If the PLQY$_{film}$ can be seen as the limit of solely bulk recombination in the device, the small difference between PLQY$_{film}$ and PLQY$_{device}$ can indicate a bulk limitation of the V_{oc}, assuming that the perovskite film morphology and crystallization is the same in both samples. We verified this by comparing the X-ray diffraction (XRD) patterns and film morphology via top- and cross sectional SEM images, as shown in Figure S2 (Supporting Information). We further checked that the PL of the perovskite film does not change substantially with the stoichiometry due to slight PbI$_2$ excess (see Figure S3, Supporting Information). In addition, the perovskite-air interface may contain undefined energy states, which could differ from the interface states present in the completed solar cell. Given that high surface recombination velocities (S) may reduce PLQY$_{film}$, causing it to deviate from the bulk limit in the device, it is crucial to measure PLQY$_{film}$ in a manner that minimizes the influence of surface recombination effects, allowing for a more accurate assessment of the bulk properties of the film material.

2.2. Analysis of Surface Recombination on the Perovskite Film on Glass

Surface recombination of charge carriers is often minimized by coating the perovskite with high bandgap interlayers or passivating molecules. It has been shown that the PLQY$_{film}$ in solution-processed perovskites can improve by such a treatment with passivation agents (up to a QFLS$_{film}$ rise of 86 meV).[13] We applied a series of frequently-used passivation agents[6,29,41,49–56] on the pristine perovskite surface and compared their PLQY$_{film}$ with a reference non-treated sample. The passivation agents, range from cations enabling the formation of low-dimensional perovskites, to ionic liquids, metal oxides, and several Lewis bases. The experimental PLQY$_{film}$ data were then used to calculate the QFLS$_{film}$ via (1) (the bandgap E_g was assumed to be constant). **Figure 2**a shows the QFLS$_{film}$ improvement for the different glass/MAPbI$_3$/passivation layer stacks, compared to the un-passivated MAPbI$_3$ film on glass. There are only marginal improvements in the QFLS$_{film}$ for some of the passivating molecules. Indeed, when considering the measurement uncertainty given by batch-to-batch variations we feel these changes are almost negligible (Figure S1b, Supporting Information). This
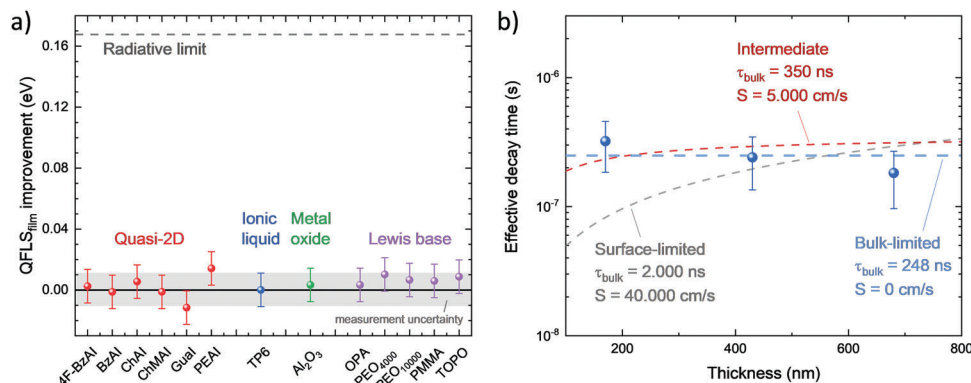
**ADVANCED
SCIENCE NEWS**

www.advancedsciencenews.com

**ADVANCED
OPTICAL
MATERIALS**

www.advopticalmat.de

Figure 2. a) Overview of the improvement in the quasi-Fermi level splitting ($QFLS_{film}$) in $MAPbI_3$ films on glass due to different passivation agents in comparison to the pristine $MAPbI_3$ film. The gray dashed line represents the improvement needed to reach the radiative limit. The colors indicate the material classes. The errors are based on the measurement uncertainty given by spot-to-spot, sample-to-samples and batch-to-batch variations of the $PLQY_{film}$. b) Effective decay times of $MAPbI_3$ films with different thicknesses (blue dots). The decay times were extracted from Figure S5b (Supporting Information) as the differential decay time at the lowest $QFLS_{film}$ measurable. The lines show the theoretical behavior of Equation 2 with different bulk lifetimes and surface recombination velocities. The blue line is the fit of the experimental data indicating no surface recombination. The black line displays a behavior in the case of a film that is limited by surface recombination. The red dashed line represents an intermediate situation. The error bars are based on the error propagation of the measurement uncertainty of the $PLQY_{film}$ and the fitting error of the TRPL decays.

lack of $QFLS_{film}$ improvement indicates that the open perovskite surface plays a minor role in the total recombination of the film. We additionally verified the effects of the solvents that were used to coat some of the passivating molecules, as summarized in Figure S4 (Supporting Information, which also contains data corresponding to few other molecules that we could not apply correctly or that destroyed the perovskite film).

Another experiment to investigate surface recombination is time-resolved PL (TRPL) on films of different film thicknesses. For weakly-doped materials such as perovskites, the charge-carrier lifetime depends on the charge-carrier concentration inside the film, and thereby on the $QFLS_{film}$.[57,58] Shallow traps, radiative, and Auger recombination lead to shorter lifetimes for higher $QFLS_{film}$. Only if deep traps dominate the charge carrier recombination in a film, the effective PL decay time will be constant at low $QFLS_{film}$, which is reached at long delay times after the excitation pulse, and a mono-exponential decay is observed. Under these conditions, the lifetime can be expressed via[58]

$$\tau_{eff} = \frac{1}{\frac{1}{\tau_{bulk}} + \frac{S}{2d}} \qquad (2)$$

As observed in the equation, the effective lifetime has two contributions, one from the perovskite bulk with the bulk carrier lifetime, τ_{bulk}, and one from the recombination at the surfaces, which scales with S, and the thickness of the film d. That means that, if the carrier recombination in the glass/perovskite sample is dominated by surface recombination, a thin film will have a shorter carrier lifetime than a thick film. In contrast, the lifetime of carriers will be constant if bulk recombination is dominant. To identify which situation occurs in the co-evaporated $MAPbI_3$ films, we performed TRPL measurements with varying laser fluence. We analyzed $MAPbI_3$ films of different thickness (170, 430, and 680 nm) deposited on glass substrates (see Experimental Section and Figure S5a–c, Supporting Information). For the data analysis, instead of fitting the curves by a pre-defined decay function, we calculated the differential decay times as a function of

the $QFLS_{film}$ for each decay curve.[30] The $QFLS_{film}$ directly after the excitation pulse is given by the laser fluence, and afterward it decays with the logarithm of the relative PL intensity at the delay time t in comparison to time zero, $kT \ln[PL(t)/PL(t = 0)]$. The differential decay time can be obtained with the derivative of the decay curve via $\tau_{eff} = -2(d\ln(PL)/dt)^{-1}$. Figure S5d (Supporting Information) shows the $\tau_{eff}(QFLS_{film})$ curves of all samples and all fluences overlayed. For each sample, the curves using different laser fluences should overlap. However, at short times after the pulse which corresponds to high $QFLS_{film}$ of each curve, drift-diffusion effects shorten the differential decay time leading to tails in Figure S5d (Supporting Information). To avoid these effects, the upper envelope of the curves (the highest τ_{eff} at a given $QFLS_{film}$) must be taken into consideration. The differential decay time τ_{eff} decreases with rising $QFLS_{film}$ as one would expect from radiative recombination or shallow traps. At low $QFLS_{film}$ values, τ_{eff} starts to exhibit a flatter behavior, indicating a deep trap, for which the lifetime is defined by Equation 2. We note that the observable range of $QFLS_{film}$ is limited by measurement noise, so that the differential decay time in Figure S5d (Supporting Information) does not yet fully saturate. We use the highest measurable decay time while pointing out that the real lifetimes are likely higher which might distort the data analysis. To check the influence of surface recombination on the samples, the extracted decay times are plotted as blue dots in Figure 2b. The dashed lines in Figure 2b show the thickness-dependent behavior of τ_{eff} following Equation 2 under three cases, where different hypothetical τ_{bulk} and S conditions are assumed for a surface: a bulk-limited and an intermediate case. The experimental values show the opposite behavior of what would be expected from a surface-recombination-dominated film, with 320, 241, and 182 ns for the 170, 430, and 680 nm thick films, respectively. While we cannot assert these values as definitive recombination lifetimes of a deep trap, the trend suggests that recombination in the bulk predominantly influences the decay process. This observation supports the conclusions drawn from the passivation study depicted in Figure 2a.

**ADVANCED
SCIENCE NEWS**

www.advancedsciencenews.com

**ADVANCED
OPTICAL
MATERIALS**

www.advopticalmat.de

We can therefore conclude that trap-assisted surface recombination does not considerably quench the PL of co-evaporated perovskites, which implies that the $PLQY_{film}$ is limited by recombination processes in the bulk of the film. The similarity in the obtained $PLQY_{film}$ and $PLQY_{device}$ (Figure 1c) suggests that also the V_{oc} of the device is at least partly limited by charge-carrier recombination in the bulk, and therefore, improvements due to interface passivation will likely be insignificant in V_{oc}.

2.3. Device Simulations

To get further insight into the limitations of our co-evaporated $MAPbI_3$ films and their effect on device performance, we predicted how the JV curve under 1 sun illumination (JV_{sun}) would change with either perfect bulk or perfect interface passivation. We established a drift-diffusion device model by globally fitting the experimental JV_{sun} curve together with pseudo-JV curves constructed from light intensity dependent data, namely the Suns-V_{oc} and the Suns-$QFLS_{film}$ curve.[13] The Suns-V_{oc} curves can be obtained by measuring the V_{oc} of the device at different light-intensities (see Figure S6, Supporting Information), converting the light intensity to the current density (where the 1-sun intensity corresponds to the short-circuit density J_{sc} at 1 sun) and subtracting J_{sc} (1 sun) to shift the curve into the fourth quadrant (dots in **Figure 3**a). Given that at open-circuit conditions no charge is extracted, the FF of the pseudo-JV curves is only limited by non-radiative recombination and shunt resistance. Therefore, the difference between the real JV_{sun} curve (black) and the Suns-V_{oc} curve (red) is due to substantial transport issues, which lead to an absolute PCE loss of 2.3% (Figure S7a, Supporting Information). The Suns-$QFLS_{film}$ curve can be obtained in a similar way as the Suns-V_{oc} curve by determining the $QFLS_{film}$ from the $PLQY_{film}$ of the free-standing perovskite film at different light intensities. The Suns-$QFLS_{film}$ curve (blue dots) provides the efficiency potential in the absence of interface limitations with the CTLs, thus the bulk-recombination limit with perfect transport. Both pseudo-JV curves are rather similar to each other, and due to transport losses considerably better than the measured JV_{sun} curves.

From the above findings, one could conclude that the interfaces with the CTLs introduce little additional recombination and that reducing the perovskite bulk traps might lead to high V_{oc} values. To examine this, we created a device model using the 1D drift-diffusion simulator SIMsalabim[59] by fitting the JV_{sun} and pseudo-JV curves together with the SQ limit for a bandgap of 1.6 eV (see solid lines in Figure 3a). The fitting procedure was to fit first the SQ limit, then the Suns-$QFLS_{film}$, the Suns-V_{oc}, and finally the real JV_{sun} curve using the parameter set that was obtained from the fitting of the previous case. For the SQ limit, ideal transport and recombination were assumed, leaving the radiative recombination rate as the only parameter that was fitted and the value was maintained for the fitting of the pseudo- and measured JV_{sun} curves. The Suns-$QFLS_{film}$ fit includes non-radiative bulk recombination and the Suns-V_{oc} fit adds non-radiative recombination from interfaces and energy alignment of the CTLs. Lastly, the measured JV_{sun} curve fits the transport properties. The model we derived has a common parameter space and leads to excellent fits with the experimental data points (Figure 3a dots and solid lines, respectively). An overview of the fitting parameters and a
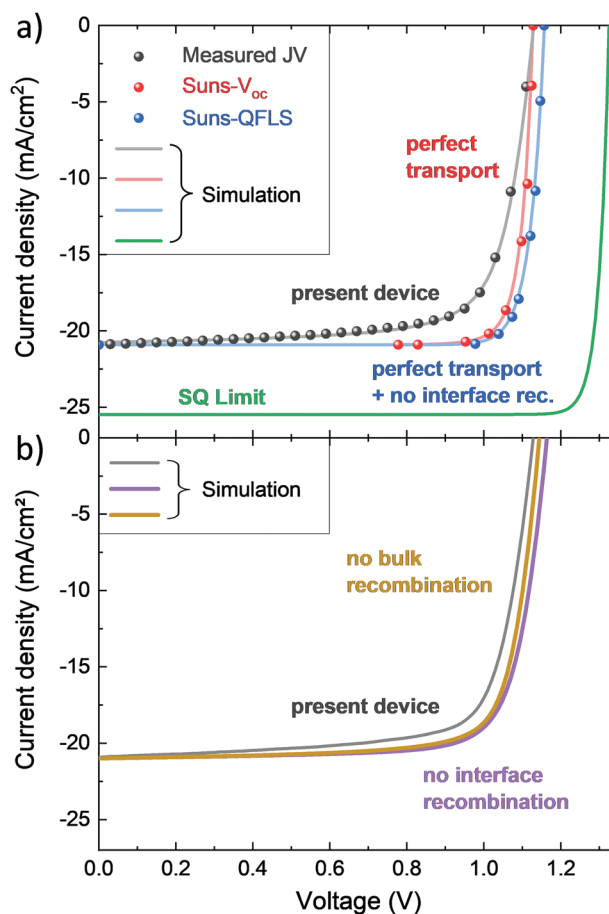

Figure 3. a) Measured JV_{sun} (black dots), suns-V_{oc} (red dots), and suns-$PLQY_{film}$ (blue dots) curves obtained from $MAPbI_3$ devices and $MAPbI_3$ films deposited on glass. The solid lines represent the simulated global fits for each situation, with the green line being the SQ limit. b) Simulated curves for the measured JV under 1 sun illumination (gray, same as *present device* in a) and assuming ideal bulk (yellow) or interface recombination (violet), but including transport limitations.

more detailed description are available in Table S1 (Supporting Information).

We then used this model and parameter set to simulate JV_{sun} curves in which the recombination of either the bulk or the interfaces is removed (Figure 3b; Figure S7b, Supporting Information). These are limiting cases in which either the bulk or the interfaces were optimized experimentally. Note that the limit of only bulk recombination is different from the Suns-$QFLS_{film}$ curve, as it still includes the transport limitations assumed in the model. Importantly, both simulated limits, bulk and interface recombination, are surprisingly similar, and closely resemble the experimental JV curve. While the V_{oc} is slightly higher when only bulk recombination is present, the efficiency of both is nearly identical and only ≈1.5% higher than the measured curve. These observations indicate that both the bulk and the interface recombination are equally limiting the devices. This implies that isolated improvements in one of them will be difficult to detect as the resulting JV_{sun} curves will be very similar. In other words, in a typical experiment involving the modification of either the
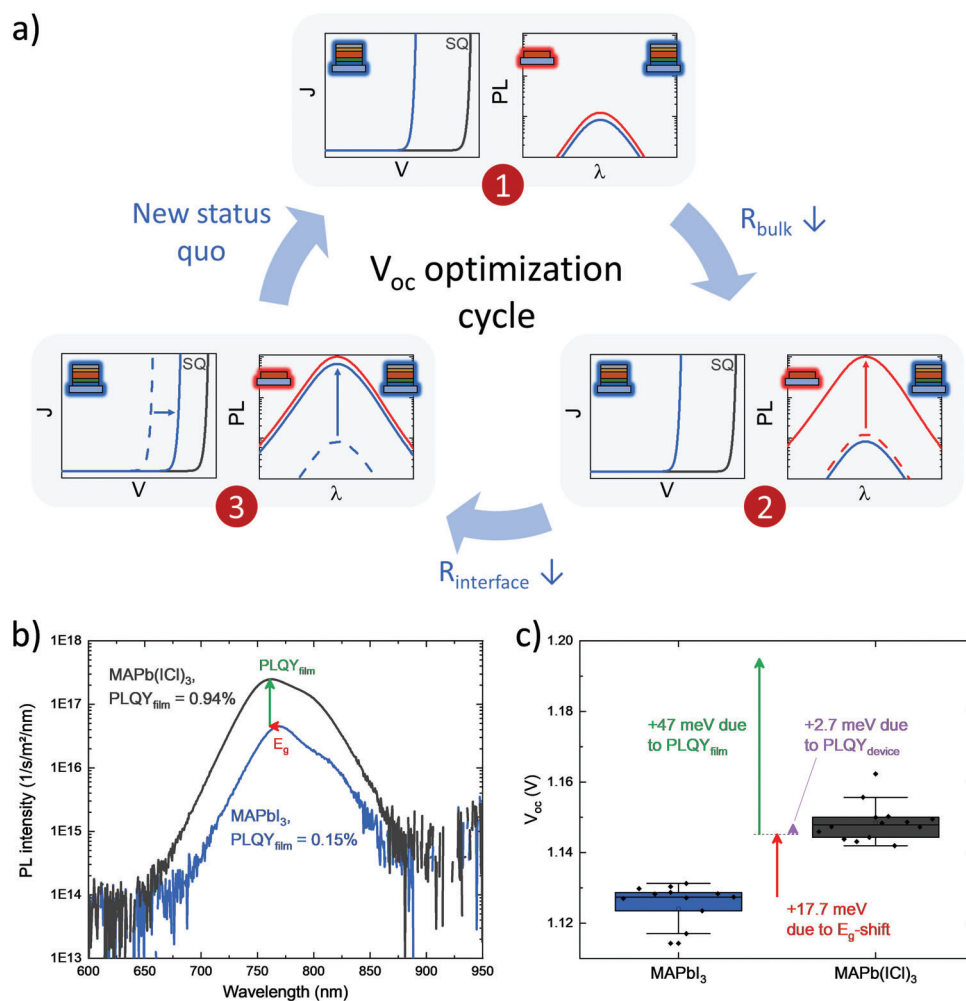
**ADVANCED
SCIENCE NEWS**

www.advancedsciencenews.com

**ADVANCED
OPTICAL
MATERIALS**

www.advopticalmat.de

Figure 4. a) Proposed cycle for V_{oc} optimization. 1) corresponds to a situation where the PLQY of the film is close to that of the device, hence the bulk of the film should be improved. This leads to situation 2) where the $PLQY_{film}$ of the film is increased but the V_{oc} of the device remains approximately the same. In step 3), the interface recombination is reduced leading to an increase in the $PLQY_{device}$ and the V_{oc}. Situation 3) is an improved situation 1), from where the optimization cycle restarts. b) PL emission spectra of $MAPbI_3$ and $MAPb(ICl)_3$, showing a bandgap shift of 19 meV (red arrow) and a $PLQY_{film}$ increase by a factor of 6.3 (green arrow) corresponding to a total $QFLS_{film}$ increase of 66 meV. c) Comparison of the V_{oc} between $MAPbI_3$ and $MAPb(ICl)_3$. The arrows show the contribution of the bandgap shift (red), the QFLS improvement due to $PLQY_{film}$ (green) and the actual V_{oc} improvement in the device due to $PLQY_{device}$ (violet).

CTLs or the perovskite bulk, even significant improvements will have minimal effects on the resulting JV_{sun} curves. Besides, if the improvement is small, it might be hidden in measurement uncertainties, hampering any device optimization. This dual contribution, unusual in the current state of solution-processed perovskites, hinders advancement in vacuum-based PCSs.

2.4. V_{oc} Optimization Cycle

To overcome this dilemma, we propose a facile and accessible strategy for V_{oc} optimization based on the combined utilization of PL and JV_{sun} measurements using two samples, the perovskite film on glass and the full device incorporating that same film (as illustrated by **Figure 4**a). This is a cycle in which any PSC takes part, independent of the performance. The decisive step that is not yet commonly represented in the device-optimizing literature

is the comparison of the PL of the film and the device. For the PL of the film sample, we assume that proper care is taken that the surface recombination of the film is minimized so that the measurement represents the bulk limit. We start illustrating this PL and JV_{sun} cycle with the situation found here in the co-evaporated $MAPbI_3$ film and solar cell (1 in Figure 4a): The device is so far optimized that it shows a diode-like rectification in the JV_{sun} curve and the PL peak of the perovskite film is only slightly more intense than the luminescence peak of the full device. In this situation, both bulk and interface recombination are similarly reducing the device V_{oc}. We propose that the first step should be to focus on reducing the traps in the perovskite bulk to increase the luminescence of the film (leading to 2 in Figure 4a). Simultaneously, the JV_{sun} of the device needs to be measured to ensure that the electronic properties of the perovskite are not compromised. In this first optimization step, we do not expect the V_{oc} to change substantially as it is most likely still limited by the interfaces.

**ADVANCED
SCIENCE NEWS**

www.advancedsciencenews.com

**ADVANCED
OPTICAL
MATERIALS**

www.advopticalmat.de

However, by changing the perovskite bulk, a change in the interface recombination might also occur which could lead to an observable change in the JV_{sun} behavior (even to a reduction in V_{oc}). After a successful, first optimization step, the film is considerably more luminescent than the device and the next step is to reduce the interface recombination. This is the current state in many solution-processed perovskites. In this situation, it is helpful to primarily identify the limiting interface of the device via PL measurements on half-stacks as discussed extensively before.[27] Once the limiting of the two interfaces is determined, the improvement of this interface will directly lead to a change in the JV_{sun} curve, and thus to an increase in V_{oc} (3 in Figure 4a). When both interfaces are optimized to the point of little quenching, it becomes more difficult to notice enhancements as discussed above, and the analysis re-starts. We want to point out that this is an iterative process and it can be applied at any stage of the solar cell optimization with the condition that the PL of both samples can be measured and that the device shows a diode-like JV curve.

In the following, we show an example of how step 1) of the device optimization could look like experimentally. MACl is a prevalent material reported in the literature to improve the bulk of perovskite films. Its effectiveness is attributed to its ability to passivate deep-level traps at the grain boundaries.[60,61] We evaluated the effect of the introduction of MACl on the bulk of MAPbI$_3$ by introducing it in the co-evaporation process. The introduction of MACl did not negatively affect the perovskite film growth which retained the tetragonal phase of MAPbI$_3$ (Figure S8a, Supporting Information). The incorporation of MACl leads to a small (19 meV) increase in the bandgap, as can be observed from the external quantum efficiency spectrum in Figure S8b (Supporting Information). This shift in the bandgap is an inevitable effect of MACl incorporation and leads to a shift in the $V_{oc,rad}(E_g)$. Figure 4b shows the PL spectra, expressed in absolute values, obtained for the MAPbI$_3$ and MAPb(ICl)$_3$ films. As clearly observed, the PLQY$_{film}$ of the MAPb(ICl)$_3$ film is significantly improved. It is 6 times higher than the MAPbI$_3$ film, corresponding to a QFLS$_{film}$ increase of 47 meV. This implies that the total QFLS$_{film}$ hence increases by ≈66 meV (by the increase in the bandgap and the increase in PLQY, 19 + 47 = 66 meV) in comparison to MAPbI$_3$. However, in the JV_{sun} curve of MAPb(ICl)$_3$ in Figure S9 (Supporting Information) we can only see a small improvement in the V_{oc} (20 mV, Figure 4c), which is much lower than the QFLS$_{film}$ increase. The substantial reduction of the bulk recombination with only a small effect on the device V_{oc} is in perfect agreement with our simulations of the MAPbI$_3$ containing solar cells. From this point, one could either try to improve the bulk further or switch to the analysis of the interfaces. This, however, goes beyond the scope of this manuscript.

3. Conclusion

In summary, with the aid of PL measurements, pseudo-JV, JV_{sun} curves and device simulations we have demonstrated that in co-evaporated MAPbI$_3$ PSCs the interface and bulk charge carrier recombination are both limiting the V_{oc}. When this is the case, the characterization of the solar cell using JV curves conceals improvements in material quality, which plausibly hinders device optimization. We used our low PLQY materials to demonstrate that a combined analysis of the PL and JV measurements

is needed to identify the limiting factors. The specific example of adding a small amount of MACl, demonstrates this. This addition leads to significant increases in the PLQY$_{film}$ but to a small increase in the V_{oc} of the device. We advocate to perform a dual analysis of the PL spectroscopy of both the film and the photovoltaic device, in conjunction with current-voltage measurements of the cell.

4. Experimental Section

Materials: ITO coated glass substrates were purchased from Naranjo Substrates. N,N,N′,N′-Tetra([1,1′-biphenyl]−4-yl)[1,1′:4′,1″-terphenyl]−4,4″-diamine (TaTm) was provided by TCI Europe N.V. Fullerene (C$_{60}$), guanidinium iodide (GuaI), cyclohexylammonium iodide (ChAI), cyclohexylmethylammonium iodide (ChMAI), benzylammonium iodide (BzAI), 4-fluoro-benzylammonium Iodide (4F-BzAI), trioctylphosphine oxide (TOPO), octylphosphonic acid (OPA), polyethylene oxide (PEO), and poly(methyl methacrylate) (PMMA) were purchased from Merck KGaA. PbI$_2$, CH$_3$NH$_3$I (MAI), MoO$_3$, 2,2′,2″-(1,3,5-Benzinetriyl)-tris(1-phenyl-1-H-benzimidazole) (TPBi) and CH$_3$NH$_3$Cl (MACl) were purchased from Luminescence Technology Corp. Phenethylammonium iodide (PEAI) was purchased from Greatcell Solar. All materials were used as received.

Device preparation: ITO-coated glass substrates were cleaned with soap, water, and isopropanol in an ultrasonic bath, followed by UV-ozone treatment. A 20 nm layer of SnO$_2$ was deposited by atomic layer deposition (ALD) using an Arradiance's GEMStar XT Thermal ALD system integrated into a nitrogen-filled glovebox as detailed before.[62] For that, the ALD chamber was heated to 90 °C; one ALD cycle consisted of consecutive purges of tetrakis(diethylamino)tin (TDAT) for 550 ms and water vapor for 200 ms, each followed by N$_2$ purges of 30 and 105 s, respectively (final growth per cycle: 1.5 Å). These substrates were later transferred to a vacuum chamber integrated into a nitrogen-filled glovebox (H$_2$O and O$_2$ < 0.1 ppm) and evacuated to a pressure of 10^{-6} mbar. Then 12 nm of C$_{60}$ was deposited followed by 500 nm of MAPbI$_3$ using quartz crystal microbalance (QCM) sensors to monitor the deposition rate. C$_{60}$ was sublimed with a deposition rate of 0.5 Å s^{-1}, while for the perovskite films MAI and PbI$_2$ precursors were simultaneously evaporated following a procedure recently published in summary, the evaporation chamber employed has only two QCMs, one close to the PbI$_2$ source designated to monitor exclusively the PbI$_2$ precursor (PbI$_2$-QCM), with no cross reading, and a second one fixed at the height of the substrates to monitor simultaneously the total amount of PbI$_2$ and MAI mass reaching the substrates (MAPbI$_3$-QCM). Initially, only PbI$_2$ was heated, and the temperature was fine-tuned to lead to a stable sublimation rate of precisely 0.50 Å s^{-1} on both PbI$_2$-QCM and MAPbI$_3$-QCM. Then, MAI was heated, and the temperature was adjusted so that the sublimation detected on the MAPbI$_3$-QCM increased from the previous 0.50 to 0.66 Å s^{-1}, while the rate on the PbI2-QCM was kept stable at 0.50 Å s^{-1}.[63] The evaporation was finished when 500 nm of MAPbI$_3$ was deposited (corresponding to ≈4 kÅ on MAPbI$_3$-QCM. The final film contains small amounts of excess PbI$_2$, which helps with the crystallization of the perovskite in the cubic phase.[63,64] In the case of devices containing MACl, a third thermal source with a corresponding QCM was simultaneously used during the MAPbI$_3$ co-evaporation at an evaporation rate of 0.05 Å s^{-1}. Then, TaTm (10 nm) and TPBi (0.5 nm) were deposited on top, followed by 6 nm of MoO3, the latter sublimed in a third vacuum chamber. To finish the device, a metal top contact of Ag (100 nm) was used. The devices were encapsulated with Al$_2$O$_3$ deposited by ALD at 40 °C similar to a protocol recently published, consisting of consecutive purges of trimethylaluminum (TMA) for 15 ms and water vapor for 150 ms, each followed by N$_2$ purges of 45 and 100 s, respectively.[65]

A similar cleaning procedure was applied to the glass substrates used for PL measurements, but in this case only the perovskite layer was deposited on the glass. Different solutions and concentrations were prepared according to previous reports found in literature. For the large ammonium cations (PEAI, BzAI, 4F-BzAI, ChMAI, ChAI), a solution

containing ≈10 mg mL⁻¹ in isopropanol was used, which was then deposited by spin-coating 100 µL at 4000 rpm. GuaI (3 mg ml⁻¹) was deposited at 5000 rpm. A solution of 6 mg mL⁻¹ TP6 in toluene was spin-coated at 4000 rpm, while PEO was prepared by dissolving 10 mg ml⁻¹ in chlorobenzene and depositing it via spin-coating at 4000 rpm. Similarly, PMMA was dissolved in chlorobenzene (1 mg mL⁻¹) and deposited at 5000 rpm. TOPO was dissolved in hexane (10 mg mL⁻¹) and deposited at 2000 rpm. In the case of OPA, 10 mg ml⁻¹ solution was prepared in hexane:tbutOH (3:1) and coated at 2000 rpm. All the layers were annealed at 100 °C for 10 min after passivation. The Al_2O_3 layer was deposited by ALD as described above.

Thin Film and Device Characterization: *Current-Voltage characterization* (JV_{sun}): The JV curve under simulated AM1.5G illumination was recorded using a Keithley 2612A SourceMeter in a −0.2 and 1.2 V voltage range, with 0.01 V steps and integrating the signal for 20 ms after a 10 ms delay, corresponding to a speed of ≈0.3 V s⁻¹. The device was illuminated under a Wavelabs Sinus 70 LED solar simulator. The light intensity was calibrated before every measurement using a calibrated Si reference diode equipped with an infrared cutoff filter (KG-3, Schott). Intensity-dependent V_{oc} measurements were obtained by placing neutral density filters, whose transmission was measured, in front of the sample.

PLQY and QFLS Calculations: The PL of the samples was measured through the glass side using a home-built setup. It was noted that this setup increases considerably the signal-to-noise ratio for materials with low PLQY compared to the commonly used method described by de Mello et al.,[66] but to perform absolute measurement of the PLQY certain considerations were assumed: i) the emission profile of all samples does not change. Due to refraction, the emission profile of light emitting diodes and solar cells was often assumed to be Lambertian; ii) the system had to be calibrated to absolute photon numbers. This requires a careful calibration of the collection path as well as the exciting light power density. To estimate the power density of the 522 nm Integrated Optics diode laser, the power was characterized with a Thorlabs PM100D meter with a S121C photodiode sensor. The spot size was defined by the D4σ method, with an Ophir SP907 beam profiling camera. Power densities between 0.4 to 61 mW cm⁻² could be reached. The collection path consists of a f = 50 mm lens for light collimation, a 600 nm long-pass filter, a fiber collimator, a 200 µm core fiber, and an Avantes Avaspec2048 spectrometer. The power was calibrated with an AvaLight-HAL-CAL-Mini calibration lamp with a known spectrum and a Lambertian emission profile.

The calibrated spectra were divided by the photon energy to receive the photon flux which was integrated numerically from 650 to 900 nm. For samples without metal back electrode, the intensity was multiplied by a factor of 2 to adjust for the outcoupling efficiency. The ratio of the obtained photon number due to emission and the absorbed photon corresponds to the external PLQY. To calculate the QFLS Equation 1 was employed from the main text where a temperature of T = 295 K was assumed. The radiative open-circuit voltage $V_{oc,rad}$ was obtained via $V_{oc,rad} = \frac{kT}{q} \ln(\frac{J_{sc}}{J_{0,rad}})$, where J_{sc} and $J_{0,rad} = q \int EQE \times \phi_{BB} \, dE$ (ϕ_{BB} being the black-body spectrum at 300 K) were the short-circuit current density and the radiative limit of dark saturation current density calculated from the EQE measurement, respectively.[65] As an example here the calculation of the MAPbI₃ film was showed which spectrum is shown in Figure 4a and Figure S1a (Supporting Information) and the PLQY in Figure 1a. The integral over the PL peak gives a total emitted photon number of $\phi_{em} = 1.89 \times 10^{18}$ 1/sm². This needs to be put in relation to the excitation photon density of $\phi_{exc} = 610$ W/m² × $(6.24 \times 10^{18}$ e/C$)$ × $(2.4$ eV$)^{-1} = 1.60 \times 10^{21}$ 1/sm² and an absorptance of 80% at 522 nm to yield an external PLQY of 0.15%. With $J_{sc} = 20.9$ mA/cm² and $J_{0,rad} = 1.1 \times 10^{-21}$ mA/cm² (see Figure S8c, Supporting Information), the radiative limit of the V_{oc} was 1.324 V. Following Equation 1, the estimated QFLS gives QFLS = $q V_{oc}$ = 1.324 eV + 0.0258 meV ln (0.0015) = 1.156 eV. A Matlab code was written to automate the data analysis.

Time-Resolved PL (TRPL): Time-resolved PL measurements were carried out using an Innolas piccolo MOPA Laser with a pulse duration of 1 nanosecond and repetition rate of 50 kHz. The samples were excited at 532 nm at moderate fluences of 8, 37 and 147 nJ cm⁻². The PL of the sam-

ples was collected by an optical telescope (consisting of two plano-convex lenses), and it was further focused on the slit of a spectrograph (PI Spectra Pro SP2300), and eventually detected with a Streak Camera (Hamamatsu C10910) system with a temporal resolution of 1.4 picosecond (ps). All samples were kept in a nitrogen-filled chamber and measured at room temperature. The data was acquired in photon counting mode using the Streak Camera software (HPDTA) and was exported to Origin Pro 2020 for further analysis. The spectra at each time delay were integrated over a small wavelength region from 746 to 803 nm (120 points). This region was chosen to maximize the signal-to-noise ratio by averaging out the noise in the signal but also keeping it small enough to not integrate over noise in weak spectra at long decay times. The obtained intensities were plotted against the delay time where the maximum was set at the time 0 and normalized to 1. Then the logarithm of the intensity φ was fitted with a 4th degree rational function. The purpose of the 4th degree rational function was solely to follow the shape of the decay accurately and avoid measurement noise. This was necessary because the effective decay time $\tau_{eff} = -2(d\ln(\phi)/dt)^{-1}$ relies on the derivative of the intensity that leads to even stronger noise if the data was noisy.[67] Finally, the QFLS was calculated from the intensity. The maximum value of the QFLS directly at the end of the laser pulse was calculated by measuring the absorbed laser fluence. From the fluence and the perovskite thickness, the absorbed photon density and from there the average charge-carrier density per volume n was calculated. It was assumed that the sample was in high-level injection at early times ($n = p$) and calculate the QFLS ΔE_F from $\Delta E_F = kT \ln(\frac{n^2}{n_i^2})$ where $n_i = 8.05 \times 10^4$ cm⁻³ is the intrinsic charge-carrier density in the MAPbI₃ perovskite.[68] Then the fact was used that there was always an exponential relation between the quasi-Fermi-level splitting and the PL flux φ, which allows to write $\phi \propto \exp(\frac{q\Delta E_F}{kT})$. This determines the QFLS at later times.

X-Ray Diffraction Measurements (XRD): The crystalline structure of the powder and film samples was studied by XRD. The patterns were collected in Bragg-Brentano geometry on an Empyrean PANalytical powder diffractometer with a copper anode operated at 45 kV and 40 mA.

Scanning Electron Microscopy (SEM): SEM images were taken with a High Resolution Field Emission Scanning Electron Microscope (HR-FESEM) ZEISS GeminiSEM 500, with a Secondary Electron In-Lens Detector using an accelerating voltage of 1KV.

External Quantum Efficiency (EQE): For the EQE measurements, the cell was illuminated by a Quartz-Tungsten-Halogen lamp (Newport Apex 2-QTH) through a monochromator (Newport CS130-USB-3-MC), a chopper at 271 Hz and a focusing lens. The device current was measured as a function of energy from 3.5 to 1.5 eV in 0.07 eV steps using a lock-in amplifier (Stanford Research Systems SR830). In bandgap region, the step size was reduced to 0.02 eV and a long-pass filter was introduced to resolve the absorption edge properly.

Device Simulation: The simulations were performed using SIMsalabim, an open-source drift-diffusion simulator for semiconductor devices, a software developed by Jan-Anton Koster et al.[59] The code can be obtained for free from https://github.com/kostergroup/SIMsalabim. The device model uses well-known parameters for MAPbI₃ and the CTLs from the literature (see Table S1, Supporting Information) to fit the Shockley-Queisser limit (SQ) assuming perfect transport and zero non-radiative recombination.[48] The only parameter that was free for fitting was the radiative recombination constant, k_{direct}, which results in a realistic value in comparison to literature.[69–72] To avoid charge transport problems, very thin CTLs and high doping concentrations were also assumed. Having the model for the SQ limit enables to fit the Suns-QFLS curve, thus the bulk recombination limit, represented in Figure 3a (blue). Assuming that the main recombination source in the bulk was at the grain boundaries,[16,17] the number of grain boundaries and their trap density were fitted. The curve was also fitted once including bulk traps, but the resulting density was so low (285 m⁻³) that was fixed to zero. The capture coefficients and trap energy level were shared parameters with the surface traps and were fitted in this step together with the doping density of the CTLs to ensure a good agreement with the pseudo-FF. At this point an asymmetry was introduced in the capture coefficients between electrons and holes. This was

**ADVANCED
SCIENCE NEWS**

www.advancedsciencenews.com

**ADVANCED
OPTICAL
MATERIALS**

www.advopticalmat.de

done, as starting points were employed for all fitting parameters that are close to literature values. After fitting the bulk recombination limit, it was proceeded to fit the Suns-V_{oc} curve by adjusting the interface trap density, the band alignment, and the doping density of the CTLs, using the real CTLs thicknesses. The obtained values, listed in Table S1 (Supporting Information), gave a very good fit to the data points previously described (see solid red curve in Figure 3a), indicative of a good model adjustment. Moreover, the JV_{sun} curve was additionally fitted with transport parameters close to the literature values (cited in the table), which lead to a good fit of the experimental curve (solid gray line in Figure 3a). To create Figure 3b, either the surface trap density or the grain boundary trap density was set to zero to construct the JV_{sun} curves for the limits with no-interface recombination or no-bulk recombination, respectively, while keeping all the other parameters of the obtained model constant.

Supporting Information

Supporting Information is available from the Wiley Online Library or from the author.

Conflict of Interest

The authors declare no conflict of interest.

Data Availabilty Statement

The data that support the findings of this study are available from the corresponding author upon reasonable request.

[1] "Best Research-Cell Efficiency Chart | Photovoltaic Research | NREL," can be found under https://www.nrel.gov/pv/cell-efficiency.html (accessed: September 2023).

[2] G. E. Eperon, S. D. Stranks, C. Menelaou, M. B. Johnston, L. M. Herz, H. J. Snaith, *Energy Environ. Sci.* **2014**, *7*, 982.

[3] S. de Wolf, J. Holovsky, S. J. Moon, P. Löper, B. Niesen, M. Ledinsky, F. J. Haug, J. H. Yum, C. Ballif, *J. Phys. Chem. Lett.* **2014**, *5*, 1035.

[4] S. D. Stranks, G. E. Eperon, G. Grancini, C. Menelaou, M. J. P. Alcocer, T. Leijtens, L. M. Herz, A. Petrozza, H. J. Snaith, *Science* **2013**, *342*, 341.

[5] L. M. Herz, *ACS Energy Lett.* **2017**, *2*, 1539.

[6] I. L. Braly, D. W. Dequilettes, L. M. Pazos-Outón, S. Burke, M. E. Ziffer, D. S. Ginger, H. W. Hillhouse, *Nat. Photonics* **2018**, *12*, 355.

[7] E. Gutierrez-Partida, H. Hempel, S. Caicedo-Dávila, M. Raoufi, F. Peña-Camargo, M. Grischek, R. Gunder, J. Diekmann, P. Caprioglio, K. O. Brinkmann, H. Köbler, S. Albrecht, T. Riedl, A. Abate, D. Abou-Ras, T. Unold, D. Neher, M. Stolterfoht, *ACS Energy Lett.* **2021**, *6*, 1045.

[8] Z. Liu, L. Krückemeier, B. Krogmeier, B. Klingebiel, J. A. Márquez, S. Levcenko, S. Öz, S. Mathur, U. Rau, T. Unold, T. Kirchartz, *ACS Energy Lett.* **2019**, *4*, 110.

[9] M. Abdi-Jalebi, M. Pazoki, B. Philippe, M. I. Dar, M. Alsari, A. Sadhanala, G. Divitini, R. Imani, S. Lilliu, J. Kullgren, M. Grätzel, R. H. Friend, *ACS Nano* **2018**, *12*, 7301.

[10] D. W. Dequilettes, S. Koch, S. Burke, R. K. Paranji, A. J. Shropshire, M. E. Ziffer, D. S. Ginger, *ACS Energy Lett.* **2016**, *1*, 438.

[11] M. Abdi-Jalebi, M. I. Dar, S. P. Senanayak, A. Sadhanala, Z. Andaji-Garmaroudi, L. M. Pazos-Outón, J. M. Richter, A. J. Pearson, H. Sirringhaus, M. Grätzel, R. H. Friend, *Sci. Adv.* **2019**, *5*, aav2012.

[12] M. Abdi-Jalebi, Z. Andaji-Garmaroudi, S. Cacovich, C. Stavrakas, B. Philippe, J. M. Richter, M. Alsari, E. P. Booker, E. M. Hutter, A. J. Pearson, S. Lilliu, T. J. Savenije, H. Rensmo, G. Divitini, C. Ducati, R. H. Friend, S. D. Stranks, *Nature* **2018**, *555*, 497.

[13] M. Stolterfoht, M. Grischek, P. Caprioglio, C. M. Wolff, E. Gutierrez-Partida, F. Peña-Camargo, D. Rothhardt, S. Zhang, M. Raoufi, J. Wolansky, M. Abdi-Jalebi, S. D. Stranks, S. Albrecht, T. Kirchartz, D. Neher, *Adv. Mater.* **2020**, *32*, 2000080.

[14] W.-J. Yin, T. Shi, Y. Yan, *Appl. Phys. Lett.* **2014**, *104*, 063903.

[15] W.-J. Yin, T. Shi, Y. Yan, *Adv. Mater.* **2014**, *26*, 4653.

[16] Z. Ni, S. Xu, H. Jiao, H. Gu, C. Fei, J. Huang, *Sci. Adv.* **2022**, *8*, 8345.

[17] Q. An, F. Paulus, D. Becker-Koch, C. Cho, Q. Sun, A. Weu, S. Bitton, N. Tessler, Y. Vaynzof, *Matter* **2021**, *4*, 1683.

[18] A. Peter Amalathas, L. Landová, Z. Hájková, L. Horák, M. Ledinsky, J. Holovský, *ACS Appl. Energy Mater.* **2020**, *3*, 12484.

[19] H. Min, D. Y. Lee, J. Kim, G. Kim, K. S. Lee, J. Kim, M. J. Paik, Y. K. Kim, K. S. Kim, M. G. Kim, T. J. Shin, S. Il Seok, *Nature* **2021**, *598*, 444.

[20] M. Stolterfoht, P. Caprioglio, C. M. Wolff, J. A. Márquez, J. Nordmann, S. Zhang, D. Rothhardt, U. Hörmann, Y. Amir, A. Redinger, L. Kegelmann, F. Zu, S. Albrecht, N. Koch, T. Kirchartz, M. Saliba, T. Unold, D. Neher, *Energy Environ. Sci.* **2019**, *12*, 2778.

[21] Z. Li, B. Li, X. Wu, S. A. Sheppard, S. Zhang, D. Gao, N. J. Long, Z. Zhu, *Science* **2022**, *376*, 416.

[22] C. M. Wolff, F. Zu, A. Paulke, L. P. Toro, N. Koch, D. Neher, *Adv. Mater.* **2017**, *29*, 1700159.

[23] J. P. Correa-Baena, W. Tress, K. Domanski, E. H. Anaraki, S. H. Turren-Cruz, B. Roose, P. P. Boix, M. Grätzel, M. Saliba, A. Abate, A. Hagfeldt, *Energy Environ. Sci.* **2017**, *10*, 1207.

[24] S. Mahesh, J. M. Ball, R. D. J. Oliver, D. P. McMeekin, P. K. Nayak, M. B. Johnston, H. J. Snaith, *Energy Environ. Sci.* **2020**, *13*, 258.

[25] J. Haddad, B. Krogmeier, B. Klingebiel, L. Krückemeier, S. Melhem, Z. Liu, J. Hüpkes, S. Mathur, T. Kirchartz, *Adv. Mater. Interfaces* **2020**, *7*, 2000366.

[26] J. Chen, N. G. Park, *Adv. Mater.* **2019**, *31*, 1803019.

[27] C. M. Wolff, P. Caprioglio, M. Stolterfoht, D. Neher, *Adv. Mater.* **2019**, *31*, 1902762.

[28] M. Stolterfoht, C. M. Wolff, J. A. Márquez, S. Zhang, C. J. Hages, D. Rothhardt, S. Albrecht, P. L. Burn, P. Meredith, T. Unold, D. Neher, *Nat. Energy* **2018**, *3*, 847.

[29] Q. Jiang, Y. Zhao, X. Zhang, X. Yang, Y. Chen, Z. Chu, Q. Ye, X. Li, Z. Yin, J. You, *Nat. Photonics* **2019**, *13*, 460.

[30] L. Krückemeier, B. Krogmeier, Z. Liu, U. Rau, T. Kirchartz, *Adv. Energy Mater.* **2021**, *11*, 2003489.

[31] J. Li, H. Wang, X. Y. Chin, H. A. Dewi, K. Vergeer, T. W. Goh, J. W. M. Lim, J. H. Lew, K. P. Loh, C. Soci, T. C. Sum, H. J. Bolink, N. Mathews, S. Mhaisalkar, A. Bruno, *Joule* **2020**, *4*, 1035.

[32] J. Ávila, C. Momblona, P. P. Boix, M. Sessolo, H. J. Bolink, *Joule* **2017**, *1*, 431.

[33] M. Liu, M. B. Johnston, H. J. Snaith, *Nature* **2013**, *501*, 395.

[34] I. Susic, L. Gil-Escrig, F. Palazon, M. Sessolo, H. J. Bolink, *ACS Energy Lett.* **2022**, *7*, 1355.

[35] B.-S. Kim, L. Gil-Escrig, M. Sessolo, H. J. Bolink, *J. Phys. Chem. Lett.* **2020**, *11*, 6852.

[36] E. Pérez-Gutiérrez, M. J. Percino, P. Santos, M. Cerón, P. Ceballos, D. M. Montoya, O. Barbosa-García, S. Thamotharan, *Mater Today Commun.* **2020**, *25*, 101384.

[37] A. M. Igual-Muñoz, A. Castillo, C. Dreessen, P. P. Boix, H. J. Bolink, *ACS Appl. Energy Mater.* **2020**, *3*, 2755.

[38] F. Meng, B. Yu, Q. Zhang, Y. Cui, S. Tan, J. Shi, L. Gu, D. Li, Q. Meng, C. Nan, *Adv. Energy Mater.* **2022**, *12*, 1.

[39] L. Gil-Escrig, C. Dreessen, F. Palazon, Z. Hawash, E. Moons, S. Albrecht, M. Sessolo, H. J. Bolink, *ACS Energy Lett.* **2021**, *6*, 827.

[40] C. Momblona, L. Gil-Escrig, E. Bandiello, E. M. Hutter, M. Sessolo, K. Lederer, J. Blochwitz-Nimoth, H. J. Bolink, *Energy Environ. Sci.* **2016**, *9*, 3456.

[41] C. Zhang, X. Ren, X. He, Y. Zhang, Y. Liu, J. Feng, F. Gao, N. Yuan, J. Ding, S. Liu, *J. Energy Chem.* **2022**, *64*, 8.

[42] H. Li, J. Zhou, L. Tan, M. Li, C. Jiang, S. Wang, X. Zhao, Y. Liu, Y. Zhang, Y. Ye, W. Tress, C. Yi, *Sci. Adv.* **2022**, *8*, 7422.

[43] T. J. Jacobsson, A. Hultqvist, A. García-Fernández, A. Anand, A. Al-Ashouri, A. Hagfeldt, A. Crovetto, A. Abate, A. G. Ricciardulli, A. Vijayan, A. Kulkarni, A. Y. Anderson, B. P. Darwich, B. Yang, B. L. Coles, C. A. R. Perini, C. Rehermann, D. Ramirez, D. Fairen-Jimenez, D. Di Girolamo, D. Jia, E. Avila, E. J. Juarez-Perez, F. Baumann, F. Mathies, G. S. A. González, G. Boschloo, G. Nasti, G. Paramasivam, G. Martínez-Denegri, et al., *Nat. Energy* **2021**, *7*, 107.

[44] F. U. Kosasih, E. Erdenebileg, N. Mathews, S. G. Mhaisalkar, A. Bruno, *Joule* **2022**, *6*, 2692.

[45] I. Levine, S. Gupta, A. Bera, D. Ceratti, G. Hodes, D. Cahen, D. Guo, T. J. Savenije, J. Ávila, H. J. Bolink, O. Millo, D. Azulay, I. Balberg, *J. Appl. Phys.* **2018**, *124*, 103103.

[46] D. Pérez-Del-Rey, L. Gil-Escrig, K. P. S. Zanoni, C. Dreessen, M. Sessolo, P. P. Boix, H. J. Bolink, *Chem. Mater.* **2019**, *31*, 6945.

[47] U. Rau, *Phys. Rev. B: Condens. Matter Mater. Phys.* **2007**, *76*, 085303.

[48] W. Shockley, H. J. Queisser, *J. Appl. Phys.* **1961**, *32*, 510.

[49] L. Zhao, N. Rolston, K. M. Lee, X. Zhao, M. A. Reyes-Martinez, N. L. Tran, Y. Yeh, N. Yao, G. D. Scholes, Y. Loo, A. Selloni, R. H. Dauskardt, B. P. Rand, *Adv. Funct. Mater.* **2018**, *28*, 1802060.

[50] P. Ferdowsi, E. Ochoa-Martinez, S. S. Alonso, U. Steiner, M. Saliba, *Sci. Rep.* **2020**, *10*, 22260.

[51] R. Zhao, K. Zhang, J. Zhu, S. Xiao, W. Xiong, J. Wang, T. Liu, G. Xing, K. Wang, S. Yang, X. Wang, *Nanoscale Adv.* **2021**, *3*, 2305.

[52] A. A. M. Brown, T. J. N. Hooper, S. A. Veldhuis, X. Y. Chin, A. Bruno, P. Vashishtha, J. N. Tey, L. Jiang, B. Damodaran, S. H. Pu, S. G. Mhaisalkar, N. Mathews, *Nanoscale* **2019**, *11*, 12370.

[53] S. G. Motti, D. Meggiolaro, A. J. Barker, E. Mosconi, C. A. R. Perini, J. M. Ball, M. Gandini, M. Kim, F. De Angelis, A. Petrozza, *Nat. Photonics* **2019**, *13*, 532.

[54] W. Sun, J. Zou, X. Wang, S. Wang, Y. Du, F. Cao, L. Zhang, J. Wu, P. Gao, *Nanoscale* **2021**, *13*, 14915.

[55] A. Q. Alanazi, M. H. Almalki, A. Mishra, D. J. Kubicki, Z. Wang, L. Merten, F. T. Eickemeyer, H. Zhang, D. Ren, A. Y. Alyamani, H. Albrithen, A. Albadri, M. H. Alotaibi, A. Hinderhofer, S. M. Zakeeruddin, F. Schreiber, A. Hagfeldt, L. Emsley, J. V. Milić, M. Graetzel, *Adv. Funct. Mater.* **2021**, *31*, 2101163.

[56] A. S. Yerramilli, Y. Chen, T. L. Alford, *Sustainable Energy Fuels* **2021**, *5*, 2486.

[57] E. Aydin, M. Bastiani, S. Wolf, *Adv. Mater.* **2019**, *31*, 1900428.

[58] T. Kirchartz, J. A. Márquez, M. Stolterfoht, T. Unold, *Adv. Energy Mater.* **2020**, *10*, 1904134.

[59] M. Koopmans, V. M. Le Corre, L. J. A. Koster, *J. Open Source Software* **2022**, *7*, 3727.

[60] K. Odysseas Kosmatos, L. Theofylaktos, E. Giannakaki, D. Deligiannis, M. Konstantakou, T. Stergiopoulos, *Energy Environ. Mater.* **2019**, *2*, 79.

[61] A. Peter Amalathas, L. Landová, Z. Hájková, L. Horák, M. Ledinsky, J. Holovský, *ACS Appl. Energy Mater.* **2020**, *3*, 12484.

[62] L. Mardegan, A. Paliwal, K. P. S. Zanoni, D. Tordera, H. J. Bolink, *Adv. Opt. Mater.* **2022**, *10*, 2201953.

[63] K. P. S. Zanoni, L. Martínez-Goyeneche, C. Dreessen, M. Sessolo, H. J. Bolink, *Sol. RRL* **2023**, *7*, 202201073.

[64] F. Palazon, D. Pérez-del-Rey, B. Dänekamp, C. Dreessen, M. Sessolo, P. P. Boix, H. J. Bolink, *Adv. Mater.* **2019**, *31*, 1902692.

[65] I. C. Kaya, K. P. S. Zanoni, F. Palazon, M. Sessolo, H. Akyildiz, S. Sonmezoglu, H. J. Bolink, *Adv. Energy Sustainability Res.* **2021**, *2*, 2000065.

[66] J. C. de Mello, H. F. Wittmann, R. H. Friend, *Adv. Mater.* **1997**, *9*, 230.

[67] T. Kirchartz, U. Rau, *Phys. Status Solidi* **2008**, *205*, 2737.

[68] F. Van Van Breugel, J. N. Kutz, B. W. Brunton, *IEEE Access* **2020**, *8*, 196865.

[69] F. Staub, H. Hempel, J. C. Hebig, J. Mock, U. W. Paetzold, U. Rau, T. Unold, T. Kirchartz, *Phys. Rev. Appl.* **2016**, *6*, 044017.

[70] T. W. Crothers, R. L. Milot, J. B. Patel, E. S. Parrott, J. Schlipf, P. Müller-Buschbaum, M. B. Johnston, L. M. Herz, *Nano Lett.* **2017**, *17*, 5782.

[71] J. M. Richter, M. Abdi-Jalebi, A. Sadhanala, M. Tabachnyk, J. P. H. Rivett, L. M. Pazos-Outón, K. C. Gödel, M. Price, F. Deschler, R. H. Friend, *Nat. Commun.* **2016**, *7*, 13941.

[72] X. Zhang, J.-X. Shen, W. Wang, C. G. Van de Walle, *ACS Energy Lett.* **2018**, *3*, 2329.